ELSEVIER

Polymer 42 (2001) 3731–3743

polymer

www.elsevier.nl/locate/polymer

Development of structural hierarchy in injection-molded PVDF and PVDF/PMMA blends
Part III. Spatial variation of superstructure as detected by small-angle light scattering

Y.D. Wang, M. Cakmak*

Department of Polymer Engineering, College of Polymer Engineering and Polymer Science, University of Akron, Akron, OH 44325-0301, USA

Received 20 June 2000; received in revised form 6 October 2000; accepted 9 October 2000

Abstract

The shape and size of the superstructure developed in spatial structural gradients formed in the injection-molded PVDF/atactic-PMMA blends were studied using small-angle laser light scattering technique. The surface layers formed due to extensional flow exhibited an unusual two-point SALS patterns when viewed in H_v mode. At high mold temperature (especially with the 70/30 PVDF/PMMA sample due to even lower nucleation density), the region between skin and shear zone that formed under relatively low stresses exhibit low nucleation density resulting in spherulitic superstructure. The inner portions of the shear layer and the core were found to form prolate spheroidal spherulites with short axis oriented in the flow direction. The aspect ratios of these spherulites are about 1.1–1.14 and this anisotropy in shape was found even at the mid-plane of the samples indicating the persistence of the influence of flow on structure at such depths. The results indicate that the mold temperature has the most influence on the evolution of superstructure in the parts as compared to the injection speed though these two parameters are not completely independent of each other. The increase of PMMA concentration drastically reduces the size of the spherulites in all depths in the molded parts. This behavior was attributed to the reduction in crystallizability particularly to the decrease of chain diffusion with the addition of stiffer non-crystallizable PMMA chains.

Keywords: Injection-molded blends; Spherulites; Small-angle scattering

1. Introduction

The injection-molded fast crystallizing polymers polyethylene (PE) [1–12], polypropylene (PP) [13–27], poly(oxymethylene) [28–31] generally exhibit multilayered morphology. At and near the skin, the nucleation density is generally high as a result of crystallization upon contact with the cold mold surface under extensional or shear stresses. The interior of the parts is generally composed of spherulitic structure whose sizes increase towards the core as the influence of stress history decreases. This qualitative description of the morphology of the injection-molded fast crystallizing polymers relies on the optical microscopy. However, the quantitative description of the size and shape of the spherulites in three-dimensional space is often found to be laborious and is almost impossible with the optical microscopy particularly when high nucleation densities are encountered. The lack of such quantitative morphological information hampers the development of quantitative modelling of superstructure evolution in injection-molding fast crystallizing polymers. One way to quantitatively describe and determine the size and shape of macro-morphology is to use the small-angle light scattering technique in cross-polarized mode (H_v).

Among the very large number of published papers, only a few cover the injection molding of PVDF [32,33], and its blends with PMMA [34]. In these publications, no structural study was undertaken investigating the influence of processing parameters and composition. Of particular interest is to investigate the effect of composition on the developed morphology that includes the average shape and size of the superstructure.

The results presented in this paper represent a part of our continuing studies on detailed analysis of the morphologies developed in injection-molded PVDF/PMMA samples using a variety of techniques including optical microscopy,

* Corresponding author. Tel.: +1-330-972-6865; fax: +1-330-258-2339.
E-mail address: cakmak@uakron.edu (M. Cakmak).

0032-3861/01/$ - see front matter
PII: S0032-3861(00)00770-9

Table 1
Materials used in this study

Polymer	Source	M_n	M_w	M_v
Poly(vinylidene fluoride)	Atochem Kynar 720	113,000	863,000	
Poly(methyl methacrylate)	Cyro Industries S10-001			110,000

thermal analysis [35] and micro-beam SAXS/WAXS techniques [36].

2. Experimental

2.1. Materials and processing

The materials and their molecular parameters are tabulated in Table 1.

A 30-mm intermeshing co-rotating JSW twin-screw extruder was used to melt blend PVDF with PMMA. The temperatures for seven zones on the extruder and the die were set to 196, 196, 198, 198, 198, 198, 198, and 200°C, respectively. The screw speed was kept constant at 90 rpm for all the blends prepared. Neat PVDF was also extruded through the twin-screw extruder in order to keep the thermo-mechanical history the same for all the samples to be studied. The concentrations of the blends are tabulated in Table 2.

As-received materials were dried in a vacuum oven at 80°C for at least 12 h to remove the moisture before the blending process and the subsequent injection-molding process.

The injection-molding process was performed using a Boy 15S injection-molding machine equipped with a standard ASTM test mold and an oil circulating mold temperature controller. The samples were prepared at two different mold temperatures (40 and 120°C) and at two different injection speeds (with the average injection flow rates of 6.9 and 34.5 cm^3/s). The rest of the processing variables including barrel temperature (195°C), injection pressure (13.8 MPa), back pressure (4.14 MPa), screw speed (165 rpm), and holding time (2 min) were kept constant. Large injection-molded tensile bars were selected for all the analysis.

2.2. Sample sectioning

In order to determine the three-dimensional shape of the spherulites, the specific locations of the samples need to be characterized at least from two mutually perpendicular views. To accomplish this, two cutting procedures were selected. In procedure C, the sample was cut from skin to core along FD (flow direction)–TD (transverse direction) plane as shown in Fig. 1. Since the steepest structure gradient is normal to the plane of this cut (along the normal direction ND) and the structural gradient in the plane is minimal, the SALS patterns of these samples were obtained directly using the conventional SALS technique.

Table 2
Compositions of the blends prepared

Blend	Concentration (PVDF/PMMA wt%)
PVDF/PMMA	100/0, 85/15, 70/30, 55/45,

The second cutting procedure, called A, consists of cutting sections of about 30 μm thickness in the ND–TD plane. These samples allow sampling with the laser beam along the FD direction. However, since ND direction contained in the plane of this cut exhibit the steepest structural gradient, the size of the sampling beam (approximately 1 mm) had to be reduced to minimize spatial averaging effects of the larger beam. However, since laser beam is Gaussian, this problem turned out to be non-trivial.

2.3. Gaussian beam optics [37]

In order to obtain the average size and shape of the spherulites at a very small step size that corresponds to increasing the probing resolution, the first technical problem we had was to reduce the diameter of the laser beam used for the small-angle light scattering study. Our goal was to reduce the beam size from 1 mm to about 100 μm using a special focusing lens. Since the laser beam is a Gaussian,

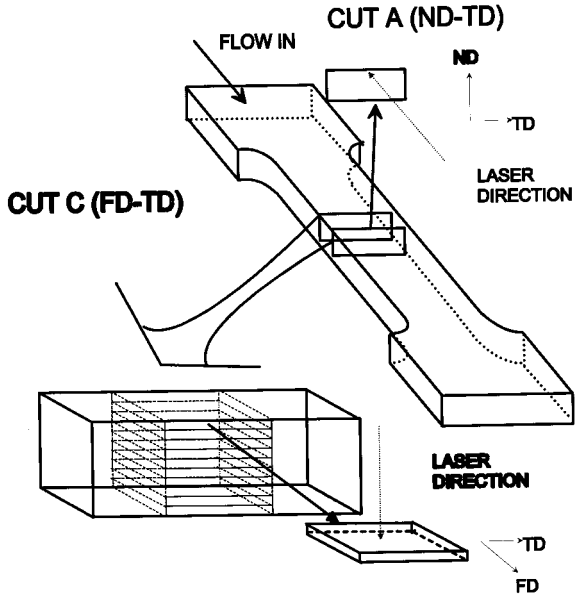

Fig. 1. Schematics of A-cut for micro-SALS and C-cut for standard SALS experiments (laser direction is indicated with dashed arrows in each experiment).

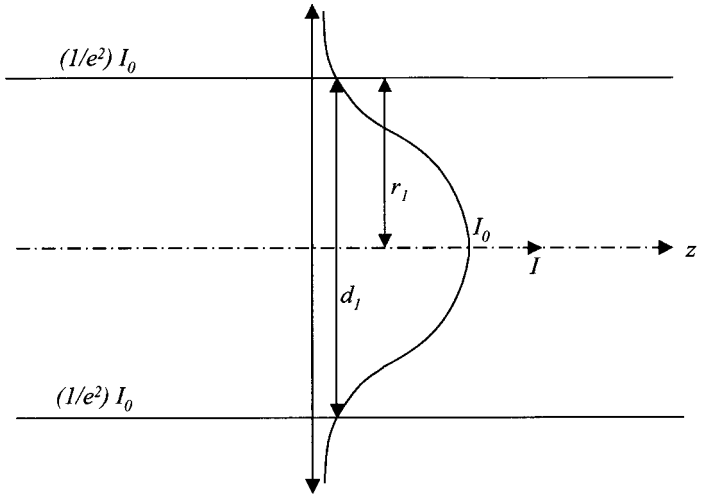

Fig. 2. Gaussian beam intensity profile. Plot of irradiance vs radial distance from the beam axis [37].

understanding of the principle of the Gaussian beam optics helped us to solve this technical problem.

The Gaussian beam is very different from the other light sources. The conventional ray optics is insufficient to explain its behavior. The design of the micro-beam small-angle light scattering system using a laser beam is a problem akin to radiometry rather than a problem in imaging.

The term "Gaussian" is used to describe the variation of the beam intensity along a line perpendicular to the direction of propagation and through the center of the beam as shown in Fig. 2. The beam is symmetric about the beam axis and its intensity $I(r)$ decreases radially outward from this symmetry axis following the Gaussian function:

$$I(r) = I_0 \, \mathrm{e}^{-2r^2/r_1^2} \tag{1}$$

The radius (r_1) or diameter of the beam is defined as the radius or the diameter of the beam where the irradiance is $1/e^2$ of the maximum value at the beam axis I_0. One significant difference between Gaussian beam and other light sources lies in the fact that a Gaussian beam either diverges from a region where the beam is smallest, called the "beam waist (d_0)", or converges to one. This is illustrated in Fig. 3. The amount of divergence or convergence is characterized by the full angle beam divergence θ, which is the angle subtended by the $1/e^2$ diameter points for distances far from the beam waist as shown in Fig. 3. For a TEM_{00} mode, d_0 and θ have the following relationship:

$$d_0 = \frac{4\lambda}{\pi\theta} \tag{2}$$

where λ is the wavelength of the radiation.

The variation of the beam diameter near the beam waist is given by the following expression:

$$d^2 = d_0^2 + \theta^2 z^2 \tag{3}$$

where d is the diameter at a distance $\pm z$ from the waist along the beam axis.

Another important term, "Rayleigh range (z_R)", is defined as the distance from the beam waist where the diameter has increased to $\sqrt{2}d_0$ as shown in Fig. 4 and is given by the following equation:

$$z_R = \frac{d_0}{\theta} = \frac{4\lambda}{\pi\theta^2} = \frac{\pi d_0^2}{4\lambda} \tag{4}$$

Through a series of derivations, the following lens equations (thin lens) for the Gaussian beam can be obtained (Fig. 5):

$$(z_2 - f)(z_1' - f) = f^2 - f_0^2 \tag{5}$$

$$f_0 = \sqrt{z_R z_R'} = \frac{d_0'}{\theta} = \frac{d_0}{\theta'} = \frac{\pi d_0 d_0'}{4\lambda} = \frac{4\lambda}{\pi\theta'\theta} \tag{6}$$

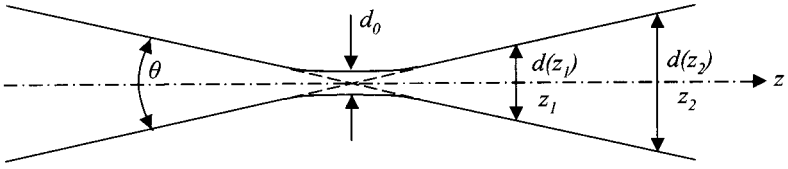

Fig. 3. Variation of Gaussian beam diameter in the vicinity of the beam waist [37].

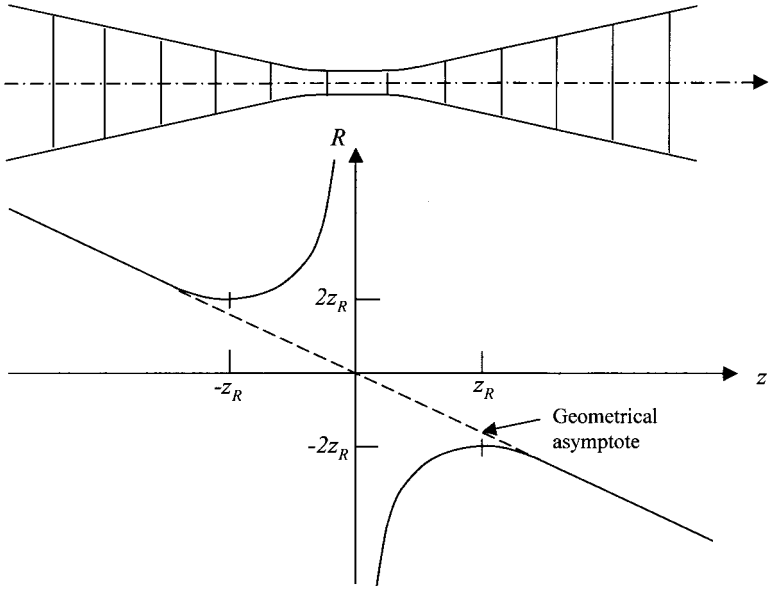

Fig. 4. Plot of radius of curvature (R) versus distance (z) from the beam waist. The absolute value of the radius is a minimum at the Rayleigh range point Z_R. In the limit of geometrical optics, the radius of curvature of the wavefronts follows the dashed line [37].

$$d_0'^2 = \frac{f^2 d_0^2}{(z_2 - f)^2 + z_R^2} = \alpha^2 d_0^2 \tag{7}$$

$$\theta' = \frac{4\lambda}{\pi d_0'} = \frac{4\lambda}{\pi \alpha d_0} = \frac{\theta}{\alpha} \tag{8}$$

$$z_R' = \frac{d_0'}{\theta'} = \frac{\alpha d_0}{\theta/\alpha} = \alpha^2 z_R \tag{9}$$

$$z_1' = f + \alpha^2(z_2 - f) = f + \frac{f^2(z_2 - f)}{(z_2 - f)^2 + z_R^2} \tag{10}$$

where f is the focal length of the thin lens, f_0^2 is introduced to account for diffraction, d_0' is the new beam waist and z_1' the position of the new beam waist. These optical relationships are used to construct a micro-SALS optical train as detailed in the following section.

2.4. Microbeam small-angle light scattering

The set-up of the microbeam small-angle light scattering system is shown schematically in Fig. 6. In this set-up, the sample is placed between two microscopic slides and mounted on a precision x–y translation stage. The x–y translation stage provides vertical and horizontal motions of the thin sample. A collimated laser beam is focused through a thin lens onto a small spot on the sample. With this set up, both H_v and V_v polarized scattering patterns can be obtained at different locations of the samples. The patterns from the samples can be captured using an instant Polaroid camera or a 16-bit CCD camera (Photometrics-cooled CCD). By simply changing the position of the lens along the optical bench, one can adjust the size of the focused beam.

In our experiment, we used a helium–neon laser with a divergence of 0.8 mrad and a thin lens with a 154.6 mm focal length, we then had from Eqs. (2) and (4):

$$d_0 = 4\lambda/\pi\theta = 1.0 \text{ mm}$$

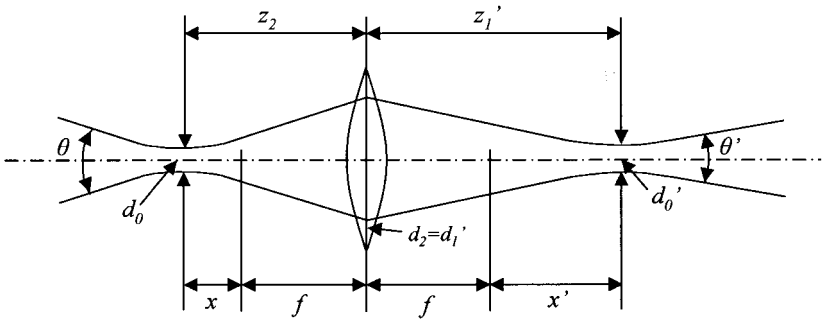

Fig. 5. Transformation of a Gaussian beam by a thin lens [37].

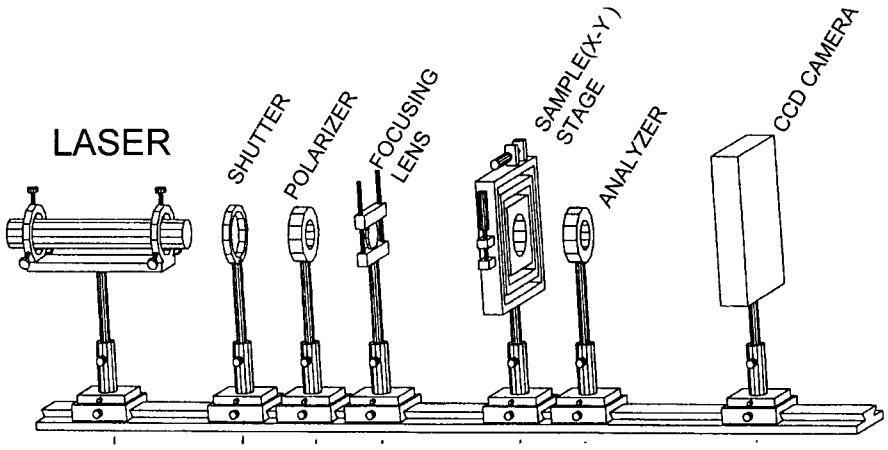

Fig. 6. Microbeam small-angle light scattering set-up: (1) laser gun; (2) shutter; (3) polarizer; (4) focusing lens; (5) x–y translator (sample mounting stage); (6) analyzer; (7) CCD camera.

and

$$Z_R = d_0/\theta = 1.25 \text{ m}.$$

We set the position of the lens at $z_2 = 300$ mm, this arrangement reduced the size of the laser beam from 1.0 mm down to about 123 μm based on the following calculation using Eq. (7):

$$d_0' = \frac{|f|}{\sqrt{(z_2 - f)^2 + z_R^2}} d_0 = 123 \text{ μm}$$

The reduction in the beam diameter was achieved at the expense of the increase in the divergence from $\theta = 0.8$ mrad to 6.6 mrad calculated using Eq. (8). This level of divergence was an acceptable compromise. In the optical train, we placed the sample at the position of the new beam waist z_1' and were able to obtain H_v scattering patterns at a series of locations from skin to core at 123 μm spatial intervals.

For the present studies, we did not obtain data in other polarization modes as we are focusing only on the size and shape of the spherulites.

2.5. Determination of the size and shape of the spherulites

Samuels [38] proposed a semi-empirical theory to predict the scattering patterns of mechanically deformed spherulites based on the equations derived by Stein and Rhodes [39] for SALS from a homogeneous anisotropic sphere in an isotropic medium (the radial arrangement of the crystallites within the spherulite giving rise to a difference in the radial and tangential polarizabilities). By using a different shape factor for an ellipsoid of revolution defined by Roess and Shull [40], Samuels could obtain the following expression for the extension ratio (λ_s) of the spherulites:

$$\lambda_s = \left[1 + \left\{ \frac{4\left[\sin^2\left(\frac{\theta_{max,1}}{2}\right) - \sin^2\left(\frac{\theta_{max,2}}{2}\right)\right]}{\sin^2\theta_{max,2}\cos^2\mu_2 - \sin^2\theta_{max,1}\cos^2\mu_1} \right\}\right]^{1/3} \quad (11)$$

where μ is the azimuthal angle and $\theta_{max,i}$ the scattering angle where the scattering intensity is maximum at a fixed azimuthal angle μ_i ($i = 1, 2$). The extension ratio of the spherulites can be calculated using Eq. (11) if $\theta_{max,1}$ and $\theta_{max,2}$ at two different fixed azimuthal angles (μ_1 and μ_2) can be experimentally determined.

The above method is somewhat inaccurate when dealing with small deformations as has been shown by Gasparyan et al. [41]. Pakula and Kryszewski [42] then proposed another method for calculating λ_s based on the same theory that Samuels used. By integrating the H_v scattering intensity over θ, Pakula and Kryszewski obtained a much simpler equation for λ_s.

$$\lambda_s = [\tan^2\mu'_{max}\tan(\mu'_{max} - \beta)\tan(\mu'_{max} + \beta)]^{1/3} \quad (12)$$

where $\beta = \arctan(1/\sqrt{2}) \approx 35°15'$ and μ'_{max} is the value of angle μ for which one observes a maximum in the scattered light intensity, integrated over θ.

The above theories predict the azimuthal position of θ_{max_0} (scattering angle where the absolute intensity maximum is observed) to be at $\mu = \pm 45°$, which may not be necessarily true.

Van Aartsen and Stein [43] proposed another three-dimensional theory to account for the density change within the spherulite (model II), the reorientation of the optic axis of the scattering element with respect to spherulite radius and the change of twist angle ω of the optic axis about the radius in the course of stretching. In their calculations, two

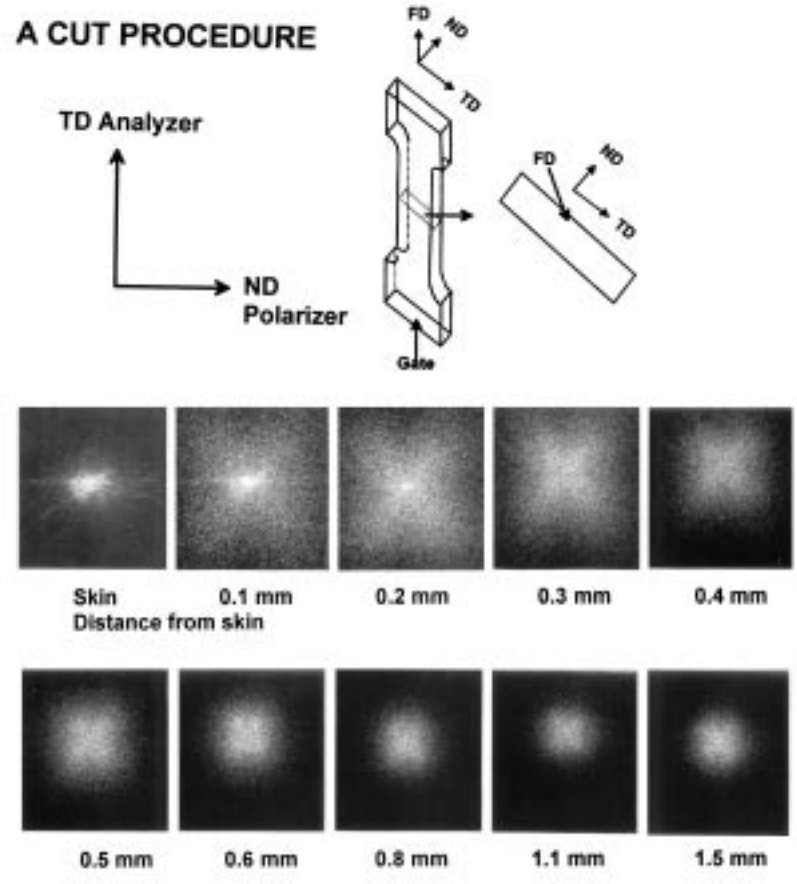

Fig. 7. Microbeam SALS H_v patterns of PVDF taken with the laser beam along the flow direction on A-cut PVDF (mold temperature, 120°C; injection speed, 6.9 cm^3/s).

types of density distribution of the scattering elements within the deformed spherulites were assumed in addition to the affine deformation. In model I, a constant density of the scattering material is preserved. In model II, the radial density of the scattering elements remains constant but the angular distribution changes affinely. Through their calculations, a fairly small difference between the predictions for the two models was found. An intermediate model was then proposed for the density distribution of the scattering material to make the mathematics simpler. A much simpler equation was then derived for calculating λ_s :

$$\cos^2 \mu_{max} = [(\lambda_s^3 + 1) \cos^2(\theta_{max_0}/2)]^{-1} \quad (13)$$

In the case of injection-molded PVDF samples, the distorted scattering patterns were also observed in the preliminary studies. The spherulites were found to be prolate spheroids with the short axis c oriented in the flow direction ($c = \lambda_3 R_0$ with λ_3 being the compression ratio and R_0 being the equivalent spherulite radius). The long axes of the spherulites a and b are oriented in the normal direction (ND) and transverse direction (TD), respectively, ($a \approx b = \lambda_1 R_0 = (\lambda_3)^{-1/2} R_0$ assuming $\lambda_1 \lambda_2 \lambda_3 = 1$). λ_1 and λ_2 are the extension ratios of the spherulites in ND and TD directions, respectively. The spherulites are similar in shape to the spherulites deformed under compression since $\lambda_3 < 1$ in this case as indicated by the experimental results shown in later section. The compression ratio (λ_3) can be calculated using Eq. (13). For small scattering angles, Eq. (13) can be further simplified as:

$$\tan \mu_{max_0} \approx \lambda_3^{3/2} \quad (14)$$

The axial ratio ($\upsilon = a/c \approx b/c$) of the spherulite can be calculated using the following equation:

$$\upsilon = \frac{a}{c} = \frac{\lambda_1 R_0}{\lambda_3 R_0} = \lambda_3^{-3/2} \approx \tan^{-1} \mu_{max_0} \quad (15)$$

Since the axial ratio found in the preliminary studies was fairly small for all the patterns obtained, the change in the equivalent radius of the spherulite (R_0) due to the distortion in the scattering pattern can be ignored. R_0 can then be estimated using the following equation [39]:

$$R_0 = \frac{\lambda}{\pi \sin \dfrac{\theta_{max_0}}{2}} \quad (16)$$

where λ is the wavelength of the laser light.

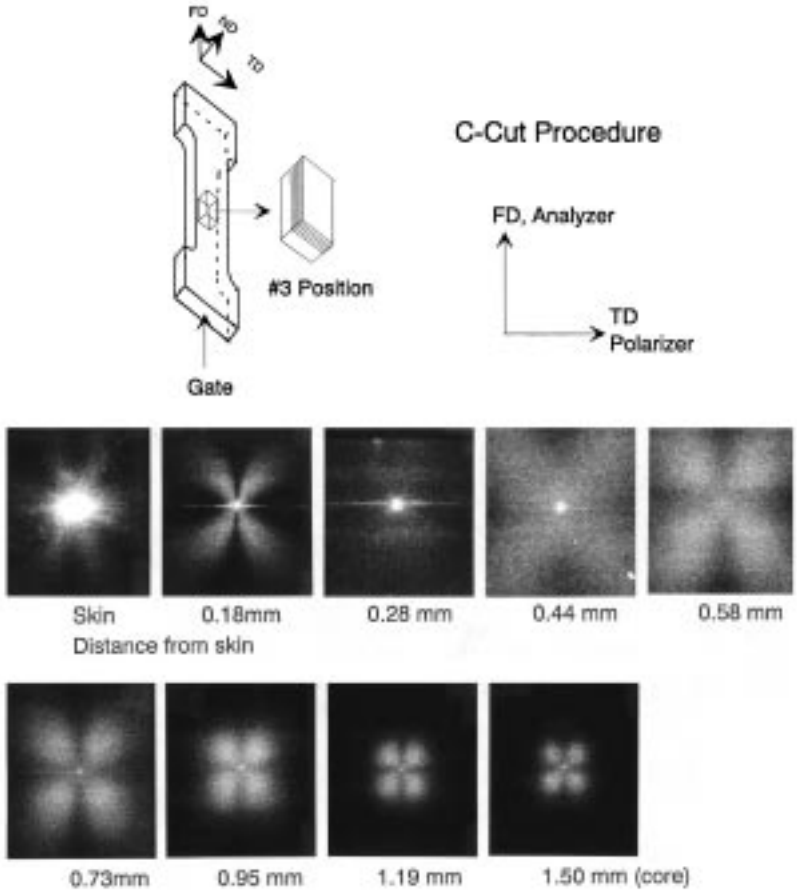

Fig. 8. SALS H_v patterns of PVDF sample cut with procedure C from skin to core (mold temperature, 40°C; injection speed, 6.9 cm^3/s).

3. Results and discussions

3.1. Microbeam small-angle light scattering studies

As indicated earlier, in order to determine the three-dimensional shape of the spherulites, one has to perform the small-angle light scattering experiments using the samples cut along at least two different planes of the sample preferably making right angles with one another. The A-cut sample (along the TD–ND plane) gives us the 2D shape of the spherulites viewed in the direction of flow (cross-sectional view). The C-cut sample reveals the 2D shape of the spherulites in the normal direction of the sample (see Fig. 1). Based on the scattering patterns obtained using the A-cut and C-cut samples at the same position of the sample, the axial ratio of the spherulites viewed in the direction along the transverse direction can be estimated.

To obtain scattering patterns using the sample cut with the A-cut procedure (cross-sectional cut), one needs to reduce the laser beam size to a level small enough to reasonably sample the morphological gradient from skin to core. With the optical set-up described above, we reduced the laser beam size from 1 mm to about 123 μm and obtained the SALS patterns at a series of small steps from skin to core with laser beam directed normal to the TD–ND plane using the A-cut sample.

Fig. 7 shows the H_v scattering patterns obtained at different locations from skin to core of the A-cut PVDF sample molded at 120°C mold temperature and at 6.9 cm^3/s injection flow rate. All the patterns presented in this figure were obtained with the same SALS optical configuration in order to illustrate spatial variation of size and shape. This figure indicates that skin layer does not show any distinguishable pattern. At about 0.1 mm from the skin that corresponds to shear crystallized regions [35,36], we begin to see the X-shaped scattering pattern with no intensity maximum in the quadrants. The intensity on each leg of the X-pattern monotonously increases towards the 0° θ scattering angle.

Beyond about 0.2 mm, the intensity maxima shift away from the 0° scattering angle that signifies the spherulitic morphology. Beyond this point that roughly corresponds to the inner boundary of the shear zone, the scattering angle decreases as the distance from skin increases indicating that the size of the spherulites increases towards the core. At the core, the size of the spherulites reaches a maximum value as expected from slower cooling that occurs away from the boundaries of the molded specimen during solidification stages of the injection molding process.

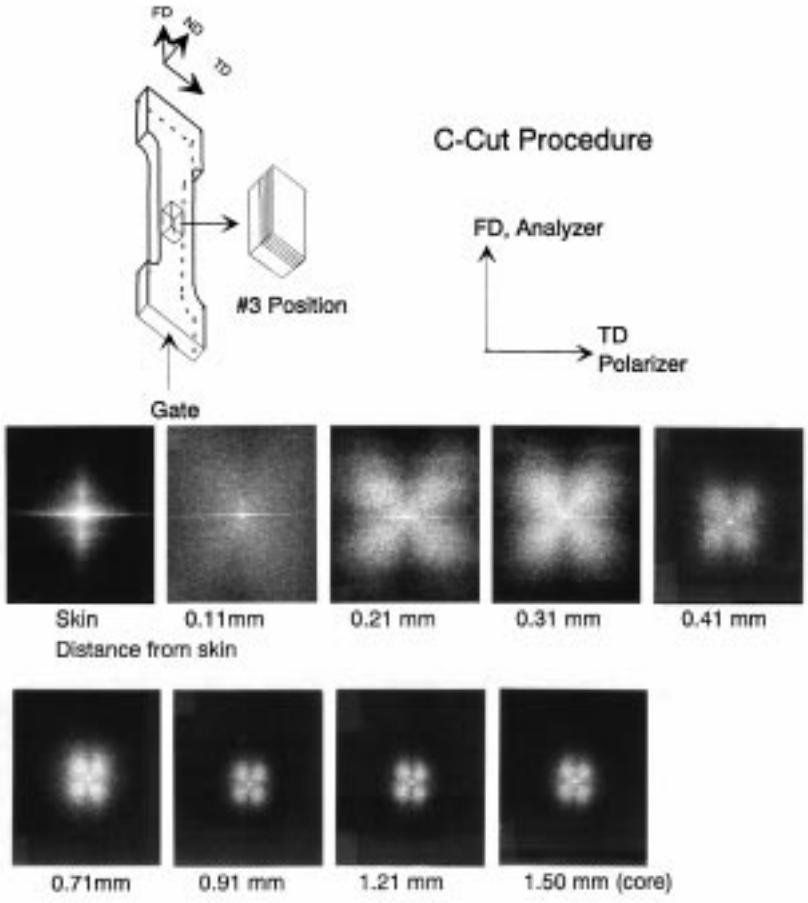

Fig. 9. SALS H_v patterns of PVDF sample cut with procedure C from skin to core (mold temperature, 120°C; injection speed, 6.9 cm^3/s).

The cross-sectional shape of the spherulites viewed in the direction of flow can be roughly estimated from these H_v scattering patterns. As can be seen from Fig. 7, the four-leaf clover H_v scattering patterns are very slightly stretched in the transverse direction indicating that the spherulites are very slightly elongated in the normal direction (thickness direction). This experimental evidence is in accord with directional crystallization that takes place under sharp thermal gradients that existed during the solidification.

In principle, we can calculate the size and the axial ratio of the spherulites from these H_v scattering patterns. However, the quality of these patterns is not good enough for any quantitative evaluation. One of the reasons for getting these poor scattering patterns is that the beam size is still too large for the region exhibiting sharp structural gradient near the surface. A beam of 123 μm in diameter may cover a region of spherulites with sizes ranging from small at one side of the beam to big at the other side of the beam. The scattering patterns obtained from a mixture of spherulites of different sizes will thus have diffuse scattering maxima. Divergence effects may have also contributed to the diffuseness of the patterns. As indicated earlier, the beam size cannot be reduced without a limit. Since the laser is a Gaussian, the reduction of the beam size can only be achieved at the expense of the increase in the divergence angle. If the beam size is too small, the divergence angle will be too large. This is also unwanted in the small-angle light scattering experiments. In addition, a beam of a very small size tends to give a speckle scattering pattern, which should also be avoided.

The best way to study the superstructural morphology of the injection-molded samples is to use the regular small-angle light scattering technique on the samples cut using the C-cut procedure (Fig. 1). In this procedure, very thin slices of less than 30 μm are microtomed parallel to the mold surface from skin to core. Due to the small thickness of these slices, the morphological gradient along the thickness direction is more accurately mapped. In this experimental orientation, the laser is directed along the thickness direction and this allows quantification of the shape and size of the spherulites in FD–TD plane (Fig. 1).

3.2. Standard small-angle light scattering studies

3.2.1. Injection-molded PVDF samples

SALS studies were performed on PVDF samples molded at two different mold temperatures (40 and 120°C) with a 6.9 cm^3/s injection flow rate. The samples were first

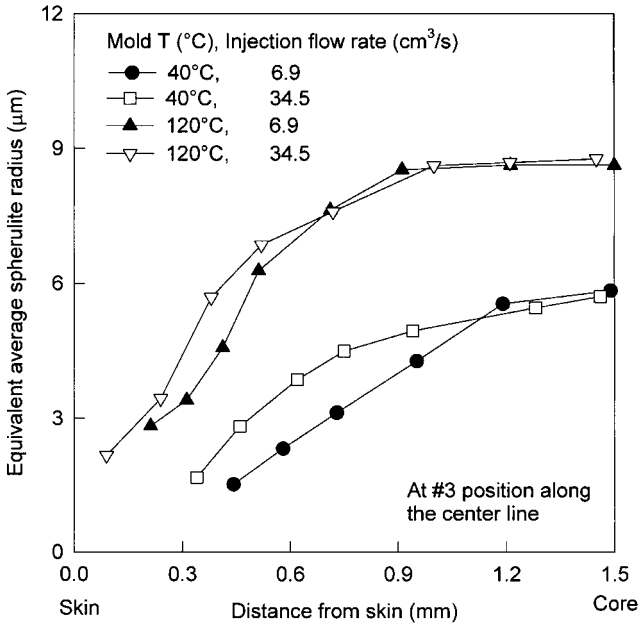

Fig. 10. Equivalent radius of spherulites vs distance from skin for PVDF samples molded under different conditions.

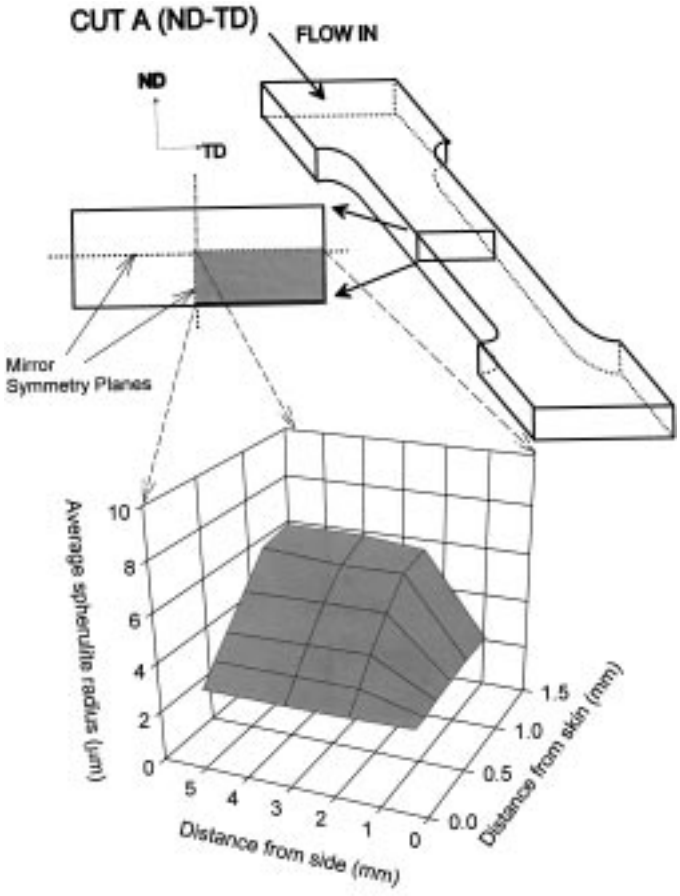

Fig. 11. Two-dimensional profile of equivalent radius of spherulites for PVDF sample molded at 40°C and at 6.9 cm^3/s injection flow rate.

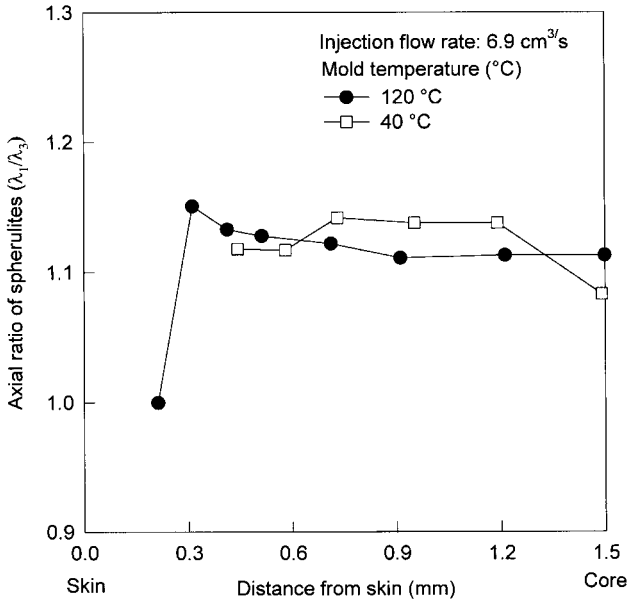

Fig. 12. Axial ratio of spherulites vs distance from skin for PVDF samples molded at 40 and 120°C mold temperatures.

microtomed into a series of layers from skin to core along the FD–TD plane. The H_v scattering pattern was then taken for each layer using the regular SALS set-up.

As an example, Fig. 8 shows the H_v patterns at different locations for the sample molded at 40°C mold temperature and at 6.9 cm^3/s injection flow rate. At 0.18 and 0.28 mm, the patterns are typical of rod-like structure where the principal polarizabilities are oriented along the rods that are at an angle to the flow direction. The X-pattern exhibit characteristically smaller angle between the arms towards FD indicating that the crystallites are elongated along the transverse direction. Starting at about 0.44 mm from the surface, four-leaf clover pattern typical of spherulitic structure emerges. This is evidenced by the movement of maximum of the scattering intensity away from the zero scattering angle. θ_{max_0} of the four-leaf clover pattern decreased towards the core indicating the expected increase of size of average spherulites with decreasing cooling rates experienced in the core of the samples. The horizontal streaks observed in the patterns corresponding to 0.18 through 0.44 are experimental artifacts caused by the parallel cutting marks left on the surfaces of the samples.

Basic morphological gradient for the sample molded at 120°C mold temperature with an injection flow rate of 6.9 cm^3/s (Fig. 9) is similar to those observed in the sample molded at the low mold temperature with one exception that the scattering patterns corresponding to the rod-like structure are concentrated closer to the skin as expected from increased mold temperature that reduces the shear layer thickness [35]. In this series of patterns, the skin exhibits a " + " pattern with maxima observed along the flow direction. The horizontal sharp streak is an artifact of cutting process as indicated earlier. And as expected, the rod-like pattern covers a small thickness range near the surface and the rest of the patterns are typical of spherulitic superstructure.

The quantitative representation of the size of the spherulites from skin to core as influenced by the injection-molding conditions for PVDF samples is shown in Fig. 10. The measurements were performed only on the patterns where clear maxima are observed in the quadrants. Because of non-spherulitic superstructure, no data for the skin and most of the shear regions are presented. In this figure, both the injection speed and the mold temperature effects are illustrated.

The samples molded at 120°C mold temperature possess larger spherulites at about the same distance from the skin than the samples molded at 40°C mold temperature as a result of the reduction in cooling rates experienced throughout the parts.

The size of the spherulites increases sharply near the surface. Surprisingly, the initial slopes of the curves are steepest in samples molded at high mold temperature. At this mold temperature, spherulite size reaches a plateau beyond about 0.9 mm. Increasing injection speed has the effect of reducing the shear layer thickness as has been observed in previous studies on other materials [44,45], mainly as a result of decreased cooling effects during the injection stage. In addition, this is further enhanced by temperature rise as a result of shear heating. As a result, the effects due to the injection speeds concentrate near the surfaces and higher injection speed results in larger spherulite size at a given depth. In the core region, the effect disappears.

In order to obtain two-dimensional profile (in ND–TD plane) of the size of the spherulites at the center of the tensile bar, we performed SALS experiments using the C-cut PVDF sample molded at 40°C mold temperature and at 6.9 cm^3/s injection flow rate. Since the sample possesses two mirror symmetry planes (one at mid-plane FD–TD and the other mid-plane FD–ND indicated by dotted lines in Fig. 11), one quadrant of the cross-sectional view would be enough to represent the full distribution of the sizes. In order to generate this distribution, we used C-cuts from skin to core and the SALS patterns were mapped in the unique quadrant indicated. As shown in Fig. 11, the size of the spherulites shows a maximum value at the spatial location where the two symmetry planes intersect at core. The gradient in the thickness direction is the steepest and towards TD this slope is much gentler at a given depth as expected.

3.2.2. Shape of the spherulites

The shape of the spherulites can be ascertained with the measurement of azimuthal angle between the lobes of the H_v pattern (μ_{max_0}). For spherical spherulites, this corresponds to 45°. This angle was found to deviate from 45° in the data shown in Figs. 8 and 9. This indicates that the shape of the spherulites is not exactly spherical at least in the view along the normal direction. The four-leaf clover patterns are

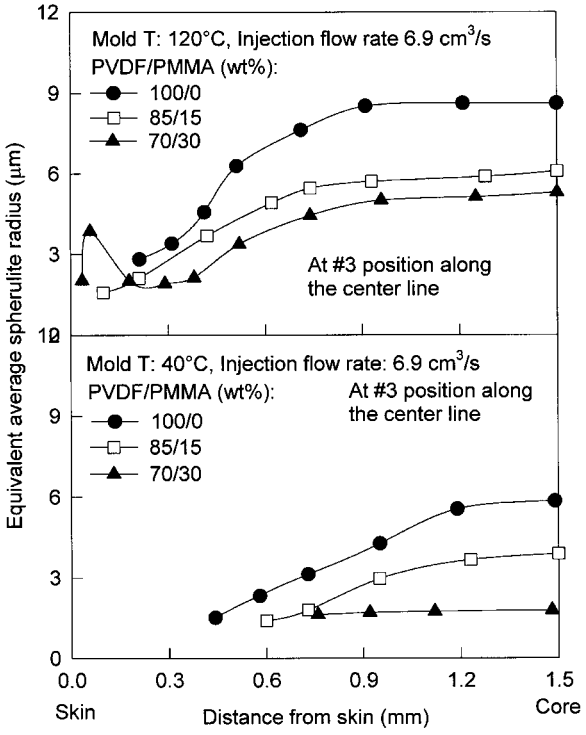

Fig. 13. Equivalent radius of spherulites vs distance for PVDF/PMMA samples molded at 40 and 120°C mold temperatures.

stretched in the flow direction. This indicates that the short axis ($c = \lambda_3 R_0$) of the ellipsoidal spherulites lies in the flow direction. The long axes of the spherulites a and b are oriented along the normal direction (ND) and transverse direction (TD), respectively, with a being slightly larger than b. However, the short axis c of the spherulites may be slightly tilted towards the core especially at positions near the shear zone as suggested by the wide-angle X-ray diffraction studies presented in the companion publication [36].

Based on the above approximation, the axial ratio ($\nu = a/c \approx b/c$) was calculated from skin to core using Eq. (15) for PVDF samples molded at 40 and 120°C mold temperatures with an average injection flow rate of 6.9 cm^3/s. As shown in Fig. 12, the axial ratio increases first and then decreases for both samples as the distance from the skin increases. The maximum axial ratio appears at a distance from skin. It is much shorter for the sample molded at the higher mold temperature since the skin and the shear layers are thinner for this sample. This anisotropy persists well into the interior of the samples reflecting the flow effects on the superstructural formation.

3.2.3. Blends of PVDF with PMMA

With the addition of PMMA, the size of the spherulites is reduced under the same injection molding condition as shown in Fig. 13. These results are consistent with our optical microscopic observations [35]. At 120°C mold temperature, we were able to measure the spherulite size very close to the skin including the shear zone. This was facilitated greatly with the reduction in nucleation density in these regions with the addition of PMMA. In fact, the location closest to the surface that we were able to make measurement approaches the skin with the increase of PMMA content. Under these conditions, the PMMA regions that may eventually be segregated into interlamellar or intercrystalline regions or both remains in rubbery state longer allowing for the development of spherulites almost all the way to skin.

The data obtained from the 70/30 PVDF/PMMA sample molded at 120°C mold temperature shows a profile of the spherulite size very different from the rest of the samples. Near the surface, between the skin and shear zone, the size profile exhibits maximum and in the shear zone, it exhibits a minimum. In injection molding of other materials including atactic polystyrene, a minimum in birefringence was observed between skin and shear zone. This was attributed to a minimum in stress levels experienced by the polymer chains during the flow and solidification. This has been proven by the birefringence measurements [46] and by the shrinkage measurements [47] on the amorphous polymers and explained based on the composite effect of the fountain flow and the shear flow [48,49]. Thus, this region may possess a lower level of nucleation density. Since this blend crystallizes at a fairly slow rate, the crystals in the region between the skin and the shear zone start to grow after cessation of the flow and before the region is completely frozen. As a result, large three-dimensional spherulites are formed under a relatively quiescent state in between the skin and shear zone.

Beyond the shear zone, the size of the spherulites increases and eventually reaches a plateau at a certain depth. The fact that these curves reach a constant value with depth despite the continuing decrease in cooling rates further towards the core suggests flow effects that determine the nucleation density persists at such depths. The observation that these spherulites exhibit anisotropy in shape even in the core confirms this effect.

The depth profile of the spherulite size in samples molded at 40°C shows a striking effect of temperature as shown in Fig. 13b. The size of the spherulites is drastically reduced in particular in the 70/30 blend, which has the highest PMMA content. Obviously, at this mold temperature, which is well below the T_g of pure PMMA, there is a drastic reduction in mobility and diffusion of chains that directly affect the number and size of the spherulites that form.

4. Summary

The skin and shear regions of the samples exhibit high nucleation densities and the morphology in general is rod-like. The SALS patterns observed in the shear zone suggests that the superstructure is made up of cross-hatched rods with the highest polarizabilities along the rod axes.

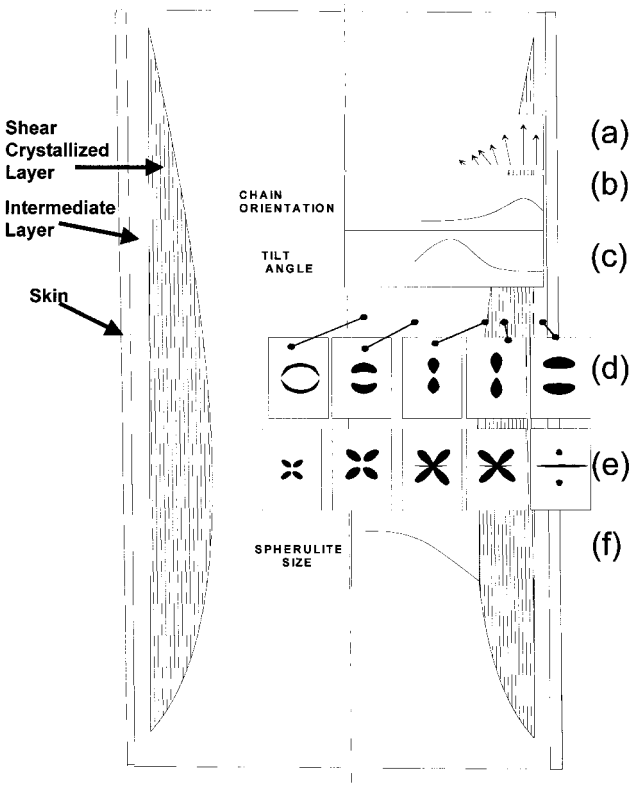

Fig. 14. Structural hierarchy in injection-molded PVDF: (a) orientation vector; (b) chain orientation; (c) tilt angle; (d) SAXS; (e) SALS; (f) spherulite size.

At high mold temperature (especially with the 70/30 PVDF/PMMA sample due to even lower nucleation density), the region between the skin and shear zone that formed under relatively low stresses exhibit low nucleation density resulting in spherulitic superstructure. The primary mechanism that controls the formation of structure in these regions is the temperature gradient.

The addition of non-crystallizable atactic PMMA certainly lowers the nucleation density at all mold temperatures investigated. As a result, the shear-crystallized zones become accessible for SALS technique while overall size of the spherulites decrease particularly when low mold temperatures are used.

5. Structural model

Overall structural hierarchy developed in the injection-molded PVDF and its blends is illustrated in Fig. 14. This model summarizes our results on micro-WAXS pole figure, SAXS results presented in the companion paper [36] and SALS results presented in this paper.

Micro-WAXS techniques allowed the quantification of the local symmetry axis orientation with respect to the macro-laboratory axis (Fig. 14a–c). At the skin, intermediate and shear crystallized layers, this axis is oriented along the flow direction. The micro-WAXS pole figure data revealed that the orientation behavior is unbalanced biaxial with strong tendency to be uniaxial near the surface. This result is specific to the mid-symmetry plane of the sample and is expected to deviate near the corners of the samples. The preferential chain orientation is moderately high at the surface layer and it was found to increase and after showing maximum at about the middle of the shear-crystallized region decreases towards the core. These local symmetry axis distribution and orientation factors are illustrated in Fig. 14a–c. Fig. 14a shows the orientation factor and orientation of the local symmetry axis in vectorial form (direction = local symmetry axis direction, amplitude: orientation of chain axes with respect to the local symmetry axes). The local symmetry axes show a tilt towards the core, a result clearly suggesting the direct influence of the flow kinematic profile on the final orientation behavior particularly at the interior near the core–shear crystallized layer boundary. This boundary clearly illustrated in this Fig. 14 is temporally and spatially established at the cessation of flow at the end of the injection cycle.

The micro-SAXS and SALS techniques certainly revealed a wealth of information on the superstructural levels. SAXS and SALS clearly established that the skin region is morphologically quite distinct from the shear region and the results illustrate that the crystallization at the skin has taken place at a very narrow temperature range as evidenced by the narrowness of the meridional distribution of the SAXS pattern. The H_v pattern at this surface layer also showed a peculiar two-point scattering pattern. The shear layers are mainly composed of the highly extended "threads" that are making up the superstructure. The SALS indicates the superstructure in this region is "rod-like" and the SAXS exhibits a very large meridional distribution of the discrete patterns. One way to interpret such results is as follows. The "threads" or "shish" regions are formed at high temperatures under the influence of the severe orientation effects that take place at the moving solid–liquid diffuse interface during the injection process. The movement of this solid–liquid interface is controlled by the temperature difference between the mold and the melt, being faster at low mold temperatures resulting in thicker so-called shear crystallized layers. However, these authors also believe that some of these "threads" may form upstream under localized stress fluctuations and carried downstream by their surrounding melt that is in the process of cooling. The reason for the meridional intensity distribution in the SAXS patterns in these regions is because of the continued crystallization of the "trapped" molten regions between the threads resulting in this "smearing" effect on the SAXS pattern as the lower temperature crystallization results in smaller crystallites and thus periodicities. The SALS results are clearly in accord with these results. The rod-like scattering pattern persists throughout the shear-crystallized region and wherever the rod-like SALS pattern is observed the meridional distribution of the SAXS pattern is also observed. The deformed spherulites that are observed in the interior are quite consistent with the above

micro-morphological structural picture. The SALS H_v patterns show that spherulite size becomes detectable starting roughly at the core–shear crystallized layer boundary. For blends especially 70/30 sample the spherulites become detectable starting from skin-shear crystallized layer boundary at the higher mold temperature. They decrease in the shear zone and towards the core. This is a clear indication that the influence of flow still persists even near the center of these samples. This suggests that the "threads" or "shishes" that represent extended chain crystallites do not disappear at the core–shear boundary but we speculate that their spatial density decrease and their presence even in the core regions results in the anisotropy in the structural hierarchy as indicated by WAXS, SAXS and SALS. Clearly, this was reflected in the three-dimensional analysis of the SALS patterns. It is shown that the spherulites are shorter in the flow direction and longer in the transverse direction and the longest in the thickness direction. This latter behavior may be a manifestation of the sharp temperature gradient in the thickness (normal direction) that enhanced the growth of the crystallites in that direction.

This series of papers represent a glimpse of how the structural hierarchy evolves in the very complex series of events that take place in injection molding. A combined structural analysis has revealed a wealth of structural information that helped elucidate some of the basic physics underlying the structural formation under complex thermal deformation conditions. These types of studies certainly need to be continued to confirm the present analysis and reveal additional details of the complex physics underlying the structural ordering processes that take place in injection molding. Once the details of the physics clearly understood, then we can begin to make headway in computational predictions of structural hierarchy.

References

[1] Tan V, Kamal MR. J Appl Polym Sci 1978;22:2341.
[2] Bakerdjian Z, Kamal MR. Polym Engng Sci 1977;17:96.
[3] Moy FH, Kamal MR. Polym Engng Sci 1980;20:957.
[4] Kamal MR, Kalyon DM, Dealy JM. Polym Engng Sci 1980;20:1117.
[5] Heckmann W, Johnsen U. Colloid Polym Sci 1974;252:826.
[6] Heise B, Killian HG, Lupke G, Schultz P, Woebcken W, Zohren J. Kolloid-Z 1972;250:120.
[7] Heise B. Colloid Polym Sci 1976;254:279.
[8] Woebcken W, Heise B. Kunststoffe 1978;68:99.
[9] Wu JP, White JL. Int Polym Process 1992;VII:350.
[10] Bayer RK, Elia AE, Seferis JC. Polym Engng Rev 1984;4:201.
[11] Bayer RK, Zachmann HG, Balta Calleja FJ, Umbach H. Polym Engng Sci 1989;29:186.
[12] Lopez Cabarcos E, Bayer RK, Zachmann HG, Balta Calleja FJ, Meins W. Polym Engng Sci 1989;29:193.
[13] Katti SS, Schultz JM. Polym Engng Sci 1982;22:1001.
[14] Kantz MR, Newman Jr. HD, Stigale FH. J Appl Polym Sci 1972;16:1249.
[15] Kantz MR. Int J Polym Mater 1974;3:245.
[16] Fitchmun DR, Mencik Z. J Polym Sci, Polym Phys Ed 1973;11:951.
[17] Mencik Z, Fitchmun DR. J Polym Sci, Polym Phys Ed 1973;11:973.
[18] Wenig W, Herzog F. J Appl Polym Sci 1993;50:2163.
[19] Trotignon JP, Verdu J. J Appl Polym Sci 1987;34:1.
[20] Trotignon JP, Lebrun JL, Verdu J. Plast Rubber Process Appl 1982;2:247.
[21] Isayev AI, Chan TW, Shimojo K, Gmerek M. J Appl Polym Sci 1995;55:807.
[22] Isayev AI, Chan TW, Gmerek M, Shimojo K. J Appl Polym Sci 1995;55:821.
[23] Saiu M, Brucato V, Piccarolo S, Titomanlio G. Int Polym Process 1992;VII:267.
[24] Ogorkiewicz RM, Weidmann GW. Plast Polym 1972;40:337.
[25] Eder G, Janeschitz-Kriegl H, Liedauer S. Prog Polym Sci 1990;15:629.
[26] Eder G, Janeschitz-Kriegl H. Colloid Polym Sci 1988;266:1087.
[27] Janeschitz-Kriegl H, Eder G. J Macromol Sci, Chem A 1990;27:1733.
[28] Clark ES. SPE (Soc Plast Engng) J 1967;23(7):46.
[29] Clark ES, Garber CA. Int J Polym Mater 1971;1:31.
[30] Clark ES. Appl Polym Symp 1973;20:325.
[31] Clark ES. Appl Polym Symp 1974;24:45.
[32] Stallings JP, Howell SG. Polym Engng Sci 1971;11:507.
[33] Trotignon JP, Verdu J, Rogues R. Morphology of polymers. Berlin: Walter de Gruyter, 1986.
[34] Mijovic J, Luo HL, Han CD. Polym Engng Sci 1982;22:234.
[35] Wang YD, Cakmak M. J Appl Polym Sci 1998;68:909.
[36] Wang YD, Cakmak M. Polymer 2000;42 (in press, this issue).
[37] O'Shea DC. Elements of modern optical design. New York: Wiley, 1985.
[38] Samuels RJ. J Polym Sci: Part C 1966;13:37.
[39] Stein RS, Rhodes MB. J Appl Phys 1960;31:1873.
[40] Roess LC, Shull CG. J Appl Phys 1947;18:308.
[41] Gasparyan KA, Holoubek J, Baranow WG, Frenkel SJ. Vysokomol Soedin A 1968;10:86.
[42] Pakula T, Kryszewski M. J Polym Sci 1972;C38:87.
[43] Van Aartsen JJ, Stein RS. J Polym Sci 1971;A2:9.
[44] Ulcer Y, Cakmak M, Miao C, Hsiung CM. J Appl Polym Sci 1996;60:669.
[45] Hsiung CM, Cakmak M, Ulcer Y. Polymer 1996;37:4555.
[46] Kamal MR, Tan V. Polym Engng Sci 1979;19:558.
[47] Menges G, Wubken G. SPE ANTEC Montreal (Canada), 1973. p. 519.
[48] Tadmor A. J Appl Polym Sci 1974;18:1753.
[49] Mavridis H, Hrymak AN, Vlachopoulos J. Polym Engng Sci 1986;26:449.